

Title Page

Structure guided *in vitro* to *in vivo* pharmacokinetic optimization of propargyl-linked antifolates

Lombardo MN^{*1}, G-Dayanandan N^{*1}, Keshipeddy S¹, Zhou W¹, Si D¹, Reeve SM¹, Alverson J³, Barney P³, Walker L³, Hoody J³, Priestley ND³, Obach RS², Wright DL¹

Department of Pharmaceutical Sciences, University of Connecticut, 69 N. Eagleville Rd., Storrs, CT
06269

Running Title Page

Running title: Pharmacokinetic optimization of propargyl-linked antifolates

Corresponding author: Dennis L. Wright, Department of Pharmaceutical Sciences, University of

Connecticut, 69 N. Eagleville Rd., Storrs, CT 06269, Email: dennis.wright@uconn.edu, Phone: (860)

486-9451

Text pages: 32

Table count: 2

Figure count: 5

Reference count: 17

Abstract: 228

Introduction: 758

Discussion: 1253

Abbreviations: AUC, area under the curve; CFU, colony forming units; CL, clearance; CL_{int} , intrinsic clearance; C_{max} , maximum plasma concentration; CYP, cytochrome P450; DHFR, dihydrofolate reductase; IC_{50} , the concentration of an inhibitor where the enzyme activity is reduced by 50%; IP, intraperitoneal; MIC, minimum inhibitory concentration; NADPH, nicotinamide adenine dinucleotide phosphate; $t_{1/2}$, half-life

ABSTRACT

Pharmacokinetic/pharmacodynamic properties are strongly correlated with the *in vivo* efficacy of antibiotics. Propargyl-linked antifolates, a novel class of antibiotics, demonstrate potent antibacterial activity against both Gram-positive and Gram-negative pathogenic bacteria including multidrug resistant *S. aureus*. We report here our efforts to optimize the pharmacokinetic profile of this class to best match the established pharmacodynamic properties. High-resolution crystal structures were used in combination with *in vitro* pharmacokinetic models to design compounds that not only are metabolically stable *in vivo* but also retain potent antibacterial activity. The initial lead compound was prone to both N-oxidation and demethylation which resulted in an abbreviated *in vivo* half-life (~ 20 minutes) in mice. Stability of leads toward mouse liver microsomes was primarily used to guide medicinal chemistry efforts so robust efficacy could be demonstrated in a mouse disease model. Structure-based drug design guided mitigation of N-oxide formation through substitutions of sterically demanding groups adjacent to the pyridyl nitrogen. Additionally, deuterium and fluorine substitutions were evaluated for their effect on the rate of oxidative demethylation. The resulting compound was characterized and demonstrated to have a low projected clearance in humans with limited potential for drug-drug interactions as predicted by CYP450 inhibition as well as an *in vivo* exposure profile that optimizes the potential for bactericidal activity highlighting how structural data, merged with substitutions to introduce metabolic stability, is a powerful approach to drug design.

INTRODUCTION

Antimicrobial drug resistance remains a top-of-mind public health concern and is often highlighted as an area of critical need for drug development. The difficulty of delivering effective antibacterial agents begins with developing lead compounds with potency against clinically relevant pathogens that also maintain optimal pharmacokinetic profiles. The importance of pharmacokinetic properties in antibiotic development lies in how crucial pharmacodynamics are to clinical effect (Jacobs, 2001). In this sense, antimicrobials are a somewhat unique therapeutic class; it is possible to directly link drug exposure to clinical efficacy through *in vitro* measurements of activity (Levinson et al., 2009). The relationship between the efficacy of antibiotics and their pharmacokinetic properties highlights the need to incorporate such work early in the drug development process.

Understanding pharmacodynamics can be extremely useful for predicting the efficacy of preclinical leads and, ultimately, in developing dosing strategies. Time-dependent antibiotics rely on maintaining an effective concentration throughout the duration of treatment. The rate and extent of antimicrobial activity is independent of drug concentrations above the minimum inhibitory concentration (MIC). Rather, it is the amount of time the plasma levels are above the MIC that is most predictive of efficacy.

Concentration-dependent antibiotics, on the other hand, exert their optimal effect through achieving the highest tolerable concentration above the MIC, meaning that C_{max}/MIC and AUC/MIC are more predictive of efficacy (Craig, 1993).

We have been developing a novel class of antimicrobials, propargyl-linked antifolates (PLAs), as effective inhibitors of the folate biosynthetic pathway. This class of agents targets the essential enzyme dihydrofolate reductase (DHFR), displaying nanomolar enzyme inhibition and exhibiting potent antibacterial activity (Scocchera et al., 2016). Structurally, PLAs are characterized by a distinct scaffold consisting of a conserved diaminopyrimidine ring connected to a biaryl system through an acetylenic linker. While the diaminopyrimidine moiety is essential for target binding to a conserved Asp/Glu residue, the acetylene-linked biaryl system allows PLAs to access key hydrophobic regions in the active

site, expanding the spectrum of activity to drug resistant enzymes (Keshipeddy et al., 2015; Lombardo et al., 2016). Crystal structures of trimethoprim-insensitive DHFRs reveal that the biphenyl system is essential for potent binding. That same biaryl system, however, diminishes the aqueous solubility of the PLAs. This issue prompted the exploration of nitrogen-containing heterocyclic derivatives such as compound **10** reported by Zhou, et al. (Zhou et al., 2012). Compound **10** not only had significantly improved physicochemical properties compared to earlier PLA derivatives but also showed potent activity against *S. aureus* with MIC values ≤ 0.625 $\mu\text{g/mL}$ (Zhou et al., 2012). It was also found that manipulating stereochemistry at the propargyl position can improve efficacy against common clinical resistance mechanisms leading to the discovery of compound **11**, an enantiomer of compound **10** (Keshipeddy et al., 2015).

With broad anti-*Staphylococcal* activity achieved, we turned our focus to characterizing and optimizing the pharmacokinetic profile of compound **11**, specifically increasing AUC levels by extending half-life and overall drug exposure. Initial *in vitro* pharmacokinetic profiling of the lead indicated that, while the acetylenic linker was metabolically stable, the compound was vulnerable to metabolism at multiple sites on the biphenyl system. In mouse liver microsomes, the racemic compound undergoes arene hydroxylation, demethylation (2'-methoxy) and N-oxidation (pyridine) with a corresponding intrinsic clearance (CL_{int}) of approximately 21 $\mu\text{L}/\text{min}/\text{mg}$ of mouse microsomal protein (Zhou et al., 2012).

The CL_{int} of the racemate forecasted a positive pharmacokinetic profile for the single enantiomer **11** *in vitro* so we moved to determine the *in vivo* pharmacokinetics of the enantiopure compound in mice. Surprisingly, the *in vivo* pharmacokinetic profile diverged significantly from the *in vitro* data, revealing a short half-life and overall poor exposure. As preliminary data indicated that intrinsic clearance was significantly lower in human liver microsomes compared to mouse liver microsomes, we used *in vitro* mouse data to guide medicinal chemistry efforts in anticipation of *in vivo* murine models of bacterial infection. In order to determine what modifications would be needed to enhance drug exposure without

compromising the strong antibacterial activity, it was first necessary to understand the source of the discrepancies between the *in vitro* and *in vivo* datasets.

In this report, we evaluate the pharmacokinetic liabilities of compound **11** and investigate strategies to decrease CYP inhibition and block the major routes of metabolism. We determined a high-resolution crystal structure of the lead in complex with the bacterial reductase and used this data to guide the synthesis of compounds with improved physicochemical properties and potent antibacterial activity. An efficient synthesis of the PLA scaffold allowed for the rapid generation of more than a dozen new analogs which enabled us to generate new, superior compounds.

MATERIALS AND METHODS

Materials. For all stock solutions, test compounds were dissolved in dimethyl sulfoxide (DMSO; Sigma-Aldrich, St. Louis, MO, USA). Buffers required for purification of recombinant DHFR were prepared with dithiothreitol (DTT), ethylenediaminetetraacetic acid (EDTA), glycerol, and Tris base purchased from Fisher Scientific (Hampton, NH, USA). Crystallization solution was prepared with gamma-butyrolactone, MES sodium salt, nicotinamide adenine dinucleotide phosphate (NADPH), polyethylene glycol (PEG) 10,000, and sodium acetate purchased from Sigma-Aldrich (St. Louis, MO, USA).

Hydroxypropyl methylcellulose (HPMC; Sigma-Aldrich, St. Louis, MO, USA) and potassium phosphate buffer (BD Biosciences, San Jose, CA, USA), was used throughout microsomal experiments. Acetonitrile (HPLC grade) was purchased from Fisher Scientific (Hampton, NH, USA). Ethyl acetate (HPLC grade) was purchased from MilliporeSigma (Burlington, MA). heptafluorobutyric acid was purchased from Sigma-Aldrich (St. Louis, MO, USA). All mobile phases were filtered using 2.0 μm filtration discs from MilliporeSigma (Burlington, MA).

Synthesis of propargyl-linked antifolates. Compounds used in this study were synthesized through a previously reported conjugate addition/Suzuki coupling protocol that allowed for efficient synthesis of racemic compounds and their corresponding enantiomeric pairs (Keshipeddy et al., 2015). Experimental and NMR spectra are provided in the Supplemental Methods.

In vitro antibacterial activity. Minimum inhibitory concentrations (MIC) were determined according to the Clinical and Laboratory Standards Institute's Performance Standards for Antimicrobial Susceptibility Testing and performed in triplicate (www.clsi.org; CLSI, 2015). The microdilution broth assay was performed using the ATCC *S. aureus* quality control strain 43300 at an inoculum of 5×10^5 colony forming units (CFU)/mL in Oxoid Iso-Sensitest Broth (ThermoFisher Scientific, Waltham, MA, USA). The MIC was defined as the lowest concentration of inhibitor to visually inhibit growth following an 18-hour incubation at 37 °C.

Time-kill assays with compound 19. Time-kill curves for compound **19** were performed in triplicate using *S. aureus* ATCC 43300. BD Difco Mueller-Hinton Broth (ThermoFisher Scientific, Waltham, MA, USA) was used throughout the experiments. Single colonies from overnight cultures grown on agar plates were added to Mueller-Hinton Broth (100 mL) and incubated at 37 °C until confluent. The bacterial suspension was adjusted to $\sim 5.5 \times 10^5$ CFU/mL (10 mL) and compound in DMSO added to give concentrations 1x (0.156 $\mu\text{g/mL}$), 5x (0.78 $\mu\text{g/mL}$), 10x (1.56 $\mu\text{g/mL}$), and 100x (15.6 $\mu\text{g/mL}$) the MIC. Samples (100 μL), taken at 0, 1, 2, 4, 6, 8, 10, 12, and 24 hours, were serially diluted in chilled normal saline and plated on Mueller-Hinton agar plates for quantification of viable colony forming units.

Cloning, expression, and enzyme purification. The gene encoding *S. aureus* DHFR was synthesized and cloned in the pET41a(+) expression vector containing a C-terminus His-tag (GenScript, Nanjing, China) as previously reported (Frey et al., 2009). Recombinant *S. aureus* DHFR was then overexpressed in One Shot BL21(DE3) Chemically Competent *E. coli* (Invitrogen, Carlsbad, CA, USA), purified via nickel affinity chromatography, and desalted using a PD-10 column (GE Healthcare, Chicago, IL, USA) into buffer containing 20 mM Tris pH 7.0, 20% glycerol, 0.1 mM EDTA, and 2 mM DTT. Recombinant protein was concentrated to ~ 10 mg/mL, flash frozen with liquid nitrogen, and stored at -80 °C.

Crystal structure determination. *S. aureus* DHFR was crystallized with NADPH and compound **11** using the hanging-drop vapor diffusion method. Purified protein (13 mg/mL) was incubated with compound **11** (2 mM) and NADPH (4 mM) for 3 hours on ice. An equal volume of protein/ligand/NADPH complex was mixed with the optimized crystallization solution consisting of 0.1 mM MES, pH 5.0, 0.1 mM sodium acetate, 13% PEG 10,000 and 20% gamma-butyrolactone additive. Crystals were observed within 14 days when stored at 4 °C. Crystals were frozen in cryo-protectant buffer containing 20% glycerol and stored in liquid nitrogen.

High-resolution diffraction data for *S. aureus* DHFR:NADPH:**11** was collected at the Stanford Synchrotron Radiation Lightsource on beamline 14-1. Data was indexed and scaled using HKL2000 (Otwinowski et al., 1997). The structure was refined and validated using noncrystallographic symmetry

and structure restraints with the PHENIX suite while COOT was used throughout the model building process (Adams et al., 2010; Emsley et al., 2010). Phaser was employed for molecular replacement using the *S. aureus* DHFR model PDB 3F0Q as a probe (McCoy et al., 2007). Inhibitor PDB and CIF files were generated with PRODRUG (Schüttelkopf et al., 2004). Data collection and refinement statistics are reported in Supplemental Table 1.

Cytochrome P450 inhibition. IC₅₀ values for recombinant human CYP3A4 were determined using a fluorescence-based high throughput inhibition assay (GENTEST; BD Biosciences, San Jose, CA, USA). Compounds were tested for inhibition activity by monitoring the conversion of 7-Benzyloxy-quinoline to the fluorescent 7-hydroxy-quinoline metabolite at 409 nm excitation and 530 nm emission. The reaction was carried out in 96-well black microtiter plates (BD Biosciences, San Jose, CA, USA). Test compounds (0.6 μL, 50 μM final concentration) were mixed with NADPH-Glucose 6-Phosphate Dehydrogenase Mix (149.4 μL) and one-third serial dilutions performed to a low concentration of 0.008 μM. The plate was pre-incubated for 10 minutes at 37 °C prior to initiation with Enzyme/Substrate Mix (100 μL). Following a 30 minutes incubation at 37 °C, the reaction was terminated with Tris Base (75 μL, 0.5 M). The concentration of test compound that corresponds to 50% inhibition were calculated by linear interpolation using the calculated percent inhibition of each compound concentration.

IC₅₀ values for recombinant human CYP2D6 were determined using a fluorescence-based high throughput inhibition assay (GENTEST; BD Biosciences, San Jose, CA, USA) where inhibition was monitored through metabolic conversion of 3-[2-(N,N-diethyl-N-methylamino)ethyl]-7-methoxy-4-methylcoumarin to the fluorescent metabolite 3-[-2-(N,N-diethylaminethyl)-7-hydroxy-4-methylcoumarin hydrochloride at 390 nm excitation and 460 nm emission. The reaction was carried out in 96-well black microtiter plates (BD Biosciences, San Jose, CA, USA) following the protocol as described for CYP3A4 IC₅₀ determination.

Microsomal stability. Microsomal CL_{int} was determined via through incubation with Male Mouse Microsomes (CD-1; BD Biosciences, San Jose, CA, USA). Test compound (2 μL) was added to reaction

buffer (973 μ L) containing 200 μ g/mL HPMC, 100 mM potassium phosphate, pH 7.4, and NADPH Regenerating System Solution (1.3 mM NADPH, 8 mM MgCl₂, 3.3 mM glucose-6-phosphate, 0.5 U/mL G6PD) to give a final test compound concentration of either 5 μ g/mL or 0.5 μ g/mL. After the mixture was prewarmed to 37 °C, the reaction was initiated with the addition of liver microsomes (25 μ L) resulting in a final protein concentration of 0.5 mg/mL. After 0, 10, 20, 30, 40, and 60 minutes, 100 μ L of sample was removed, and the reaction was terminated with equal parts ice-cold acetonitrile (ACN). Samples were subsequently centrifuged 10,000 x g for 10 minutes, and the supernatant withdrawn. Samples (5 μ L) were injected onto a Shimadzu Nexera UHPLC system equipped with a DGU-20A5 Prominence degasser, SIL-30AC Nexera autosampler, CTD-30A Nexera column oven, two LC-30AD pumps (Shimadzu, Kyoto, Japan), LCMS-2020 mass spectrometer, and a Kinetex C18 column (1.7 μ m, 100 \AA , 2.1 x 50 mm; Phenomenex, Torrance, CA, USA). The following chromatographic methods were developed to optimize resolution and detection of PLAs. Mobile phase A (0.01% heptafluorobutyric acid (HFBA) in water) and mobile phase B (0.01% HFBA in ACN) were used for a binary gradient elution that began at 95% A and 5% B, then increased to 95% B over 7 minutes, held at 95% B for 2 minutes, then decreased 5% B over 1 minute, and held at 5% B for 2 minutes.

The mass spectrometer was set to a nebulizing gas flow of 1.5 L/min, a drying gas flow of 15 L/min, the desolvation line at 250 °C, the heat block at 400 °C, and the interface temperature at 350 °C. MS was performed in the positive ion mode with EPI and APCI dual ionization mode using diltiazem (0.5 μ g/mL) as an internal control. The half-life, calculated via quantification based on MS area under the curve responses and comparison to authentic standards, was converted to give intrinsic clearance (CL_{int}).

Metabolite identification for compound 12. Phase I and phase II metabolites were identified via mouse liver S9 fractions (BD Biosciences, San Jose, CA, USA) as the source of membrane bound drug metabolizing enzymes. For generation of CYP and uridine glucuronosyl transferase (UGT) metabolites, test compound (2 μ g/mL) was supplemented with NADPH Regenerating System Solution (1.3 mM NADPH, 8 mM MgCl₂, 3.3 mM glucose-6-phosphate, 0.5 U/mL G6PD) and UGT Reaction Mix (25

$\mu\text{g/mL}$ almethicin, 2 mM UDPGA) in 100 mM potassium phosphate, pH 7.4, and HPMC (200 $\mu\text{g/mL}$) to aid in compound solubility. After the mixture was prewarmed to 37 °C, the reaction was initiated with the addition liver S9 (0.5 mg/mL). Timepoints were collected at 0 and 2 hours, quenching the reaction with equal parts of ice-cold acetonitrile (ACN). Metabolites were reconstituted in 50% methanol via SPE isolation using Oasis HLB Cartridges (Waters, Milford, MA, USA).

Samples were analyzed at the Yale School of Medicine Proteomics Center with the help of Dr. Tukiet Lam using tandem LC-MS/MS on a ThermoScientific LTQ Orbitrap XL (ThermoFischer Scientific, Waltham, MA, USA) fitted with a Waters ACQUITY UPLC System (Waters, Milford, MA, USA) and Restek Ultra AQ C18 column (3 μm , 10 mm x 1.0 mm, Particle Size: 3 μm ; Restek, Bellefonte, PA, USA). Metabolites were resolved using a gradient of 0.01% HFBA in water (A) and ACN (B). The gradient started with 0% B and increased to 100% B over 17 minutes followed by an isocratic hold at 100% B for 5 minutes at a flow rate of 75 $\mu\text{L}/\text{min}$ and the injection volume set to 8 μL . Resolution was set to 30,000. Collision energy was set to 35 eV. The collision gas was helium.

Stability of compound 17 in human hepatocytes. The intrinsic clearance of compound **17** was measured in mixed sex pooled cryopreserved human hepatocytes. Aliquots (45 μL) of human hepatocytes at a cell density of 500,000 cells/mL were suspended in Williams E medium to a final volume of 200 μL in a 96-well plate with a final substrate concentration of 1 μM . Incubations were carried out at 37 °C under an atmosphere of 95% O₂, 5% CO₂, 75% humidity on a rotating shaker. Sample aliquots (25 μL) were taken at 0, 0.5, 1, 2, 3, and 4 hours and added to 75 μL of chilled ACN plus internal standard. Samples were centrifuged at 10,000 g at 4 °C for 10 minutes, supernatant collected, loaded on to a Kinetex C18 column (1.7 μm , 100Å, 2.1 x 50 mm) and analyzed via LCMS as previously described. The percent of parent remaining (log-transformed) over time was used in a linear regression analysis to estimate half-life (first-order) which was used in subsequent calculations of intrinsic clearance.

Metabolite identification for compound 17. The *in vitro* metabolites of compound **17** were determined by LC-MS/MS following incubation with mixed sex pooled cryopreserved mouse and human hepatocytes

(Bioreclamation IVT, Westbury, NY, USA). Thawed hepatocytes were suspended in Williams E medium (ThermoFisher Scientific, Waltham, MA, USA) at a final concentration of 750,000 viable cells/mL as determined by trypan blue staining. Incubations were initiated with the addition of compound in DMSO (10 μ M) to an aliquot of cell suspension (1 mL). Samples were incubated at 37 °C under an atmosphere of 95% O₂, 5% CO₂, 75% humidity with shaking (50 rpm) in a HERAcell 240i incubator (ThermoFischer Scientific, Waltham, MA, USA). Following 45 minutes, an aliquot (500 μ L) was added to chilled ACN (2 mL) in order to capture early primary metabolites. At 4 hours, the remaining sample (500 μ L) was crashed with chilled ACN (2 mL) and combined with the early timepoint. Samples were centrifuged at 10,000 g at 4 °C for 10 minutes and supernatant collected. Samples were dried overnight using a GeneVac EZ 2 Plus Personal Solvent Concentrator (Genevac Ltd, Valley Cottage, NY, USA).

Samples were reconstituted in 0.1% formic acid in water (200 μ L) and analyzed by LC-MS/MS using a Thermo Orbitrap Elite mass spectrometer (ThermoFisher Scientific, Waltham, MA, USA) coupled to a Waters ACQUITY UPLC System (Waters, Milford, MA, USA) with a Restek Ultra AQ C18 column (3 μ m, 10 mm x 1.0 mm, Particle Size: 3 μ m; Restek, Bellefonte, PA, USA). Electrospray ionization in positive mode was used, recording full scans (m/z 100–1000), targeted, and data dependent MSⁿ at high resolution (30,000) as needed. Metabolites were resolved using a gradient of 0.1% formic acid in water (A) and ACN (B). Samples (10 μ l) were injected and a linear gradient was applied to 90% B over 35 minutes followed by a hold at 90% B for 5 minutes before returning to initial conditions and re-equilibrating for 5 minutes.

In vivo pharmacokinetic characterization of compound 19.

Animals. Experimental procedures were performed according to Institutional Animal Care and Use Committee (IACUC) protocol AUP022-14 which was approved by The University of Montana and its Institutional Animal Care and Use Committee. NIH Guidelines for the Care and Use of Laboratory Animals were followed for all experiments. Thirteen to fifteen-week-old female, CD1 mice (Envigo, Huntingdon, United Kingdom) were housed in static micro isolated cages under pathogen free, HEPA-

filtered conditions. Other housing conditions were as follows: 12-hour light/dark cycles, controlled temperature (20.5–22.5 °C) and humidity (25–45%), with weekly cage changes of bedding. Food and water were provided ad libitum. After animal delivery, animals were given at least three days to acclimate to their new environment prior to the start of any experiments.

Compound **19** was formulated for intraperitoneal (IP) delivery at a concentration of 0.2 mg/mL as follows: 1.8 mg compound **19** was dissolved in 0.180 mL of N-methylpyrrolidone (NMP), 2.0 mL of 45% w/v (2-hydroxypropyl)- β -cyclodextrin in phosphate buffered saline (PBS), and 6.820 mL of PBS. Five mice were used in the study and the average mouse weight was 34 g. Blood samples were collected via the saphenous vein into heparinized capillary tubes followed by transfer to 1.5 mL Eppendorf tubes with EDTA (30 μ L of 100 mM EDTA at pH 8) and mixed. Blood was not taken more than three times from any one mouse. Samples were stored at 0 °C until centrifuging later that same day. Following the last time point, all blood samples were centrifuged at 13,500 rpm for 15 minutes at 4 °C. The supernatant was then transferred to a new 1.5 mL Eppendorf tube and stored at –80 °C until the sample extraction step.

Sample extraction procedure. For each plasma sample a small volume (20 μ L), held in an Eppendorf tube, was mixed briefly by vortexing with internal standard (IS) spiking solution (10 μ L); the IS spiking solution consisted of 500 ng/mL 6-ethyl-5-[5-(4-pyridyl)pent-1-ynyl]pyrimidine-2,4-diamine. The samples were vortexed for 3 minutes. Ethyl acetate (500 μ L) was added to each sample, mixed by vortexing, shaken for 10 minutes, vortexed briefly again and then the phases separated by centrifugation at 10,000 rpm for 10 minutes at room temperature. The ethyl acetate supernatant (450 μ L) was transferred to a new Eppendorf tube and concentrated to dryness in vacuo using a Savant SpeedVac (ThermoFisher Scientific, Waltham, MA, USA). The dried samples were reconstituted in HPLC mobile phase (50 μ L) for analysis.

Preparation of calibration standards and quality control standards. The primary, standard stock solution of compound **19** was prepared at a concentration of 6.4 mg/mL in DMSO. The standard spiking solutions were prepared in 50:50 v/v acetonitrile:water at concentrations of 500, 1,000, 2,500, 5,000, 10,000,

20,000, 40,000, and 80,000 ng/mL. The IS stock solution was prepared at a concentration of 2.5 mg/mL in 50:50 v/v acetonitrile:water from which the IS spiking solution was prepared at a concentration of 500 ng/mL in 50:50 v/v acetonitrile:water. Standard spiking solutions and IS spiking solution were stored at $-20\text{ }^{\circ}\text{C}$ or $4\text{ }^{\circ}\text{C}$ until use. Plasma standards were prepared by adding 11 μL of respective standard spiking solution to 99 μL of drug-free mouse plasma. The working standard concentrations for plasma standards were thus 50, 100, 250, 500, 1000, 2000, 4000, and 8000 ng/mL.

Instrumentation. Analysis was performed on an Agilent HPLC system (Agilent Technologies, Santa Clara, CA, USA) equipped with an autosampler (Agilent 1260 Infinity, Model G1329B), a degasser (Agilent 1200, Model G1379B) and a binary pump (Agilent 1200, Model G1312B) coupled to a Bruker Amazon SL ion trap mass spectrometer (Bruker, Billerica, MA, USA). Data was analyzed using the Bruker Compass DataAnalysis software suite (Version 4.2, Build 383.1). A Phenomenex Gemini (3.0mm \times 150 mm, 100 \AA , 5 μm) column with an attached Phenomenex SecurityGuard (C18, 4 \times 2.0 mm, Part No. AJ0-4286; Phenomenex, Torrance, CA, USA) guard column was used for analysis. The analysis was performed under isocratic conditions at ambient temperature. The mobile phase was premixed at a ratio of 30:70 (v/v) 10 mM NH_4HCO_3 :acetonitrile. The mobile phase was filtered through 2.0 μm filtration discs (Millipore, Cat. No. AP2504700). The flow rate used was 0.320 mL/min with a resultant backpressure of approximately 35 bar. The total run time was 6 minutes with an injection volume was 10 μL .

Detection was performed with positive mode electrospray ionization (ESI) and selected ion monitoring (SIM). The $[\text{M}+\text{H}]^+$ ions at m/z 406.2 and 282.2 were chosen for SIM data collection for quantitation of **19** and the internal standard 6-ethyl-5-[5-(4-pyridyl)pent-1-ynyl]pyrimidine-2,4-diamine, respectively. The following MS parameters were used during data collection: electrospray voltage +4,500 V, source temperature $250\text{ }^{\circ}\text{C}$, nebulizer gas (nitrogen) 29 psi, and dry gas flow rate (nitrogen) 12 L/min.

RESULTS

***In vivo* pharmacokinetics for compound 11.** Plasma profiles of compound **11**, both through IP injection and oral gavage, were determined in mice using a single dose of 16 mg/kg. Following IP injection at 16 mg/kg, the C_{max} reached 10.2 µg/mL and the AUC, 294 min*µg/mL. CL and *t*_{1/2} were 54 mL/min/kg and 20 min, respectively. When administered orally at 16 mg/kg, the C_{max} and AUC were 1.44 µg/mL and 24.6 min*µg/mL giving a bioavailability of 8.4%.

Crystal structure of *S. aureus* DHFR in complex with NADPH and compound 11 and design of new analogs. Diffraction data yielded a 2.24 Å resolution structure of SaDHFR:NADPH:**11**. As expected, the diaminopyrimidine ring formed conserved hydrogen bonds with the carboxyl group of Asp 27 and the carbonyl groups of Leu 5 and Phe 92 (see Figure 1). The methoxyphenyl moiety is positioned in a predominately hydrophobic pocket consisting of Leu 20, Ser 49, Ile 50 and the cofactor, NADPH. The pyridine ring is surrounded by four hydrophobic residues (Leu 20, Leu 28, Ile 50, Leu 54) while forming a water network of hydrogen bonds with Arg 57. The 1, 2, and 6-positions of the pyridyl group are solvent exposed, suggesting that modifications in this domain would be well tolerated by the enzyme.

***In vitro* optimization of compound 11 leads to the development of compound 19.** Microsomal stability was determined for compounds **11**, **12**, and **13** by monitoring the presence of compound after incubation in mouse liver microsomes (see Table 1). The experiments were carried out with a substrate concentration of 0.5 µg/mL giving an observed CL_{int} of 10 µL/min/mg of mouse microsomal protein for compound **11**. Surprisingly, both compounds **12** and **13** had elevated clearances relative to **11** (40 and 173 µL/min/mg, respectively) despite the presence of bulky ortho substitutions designed to reduce the rate of formation of the N-oxide metabolite.

Of the CYP450 isoforms, CYP3A4 and CYP2D6 account for 50% and 30% of all xenobiotic metabolism, and play an important role in monitoring the potential for drug-drug interactions throughout the drug discovery process (Sun et al., 2011). As such, CYP3A4 and CYP2D6 IC₅₀ values were determined in

parallel by monitoring conversion of a non-fluorescent substrate to a fluorescent metabolite and calculated from the net fluorescent signal. Compound **11** was determined to have potent CYP inhibition capability (CYP3A4 IC₅₀: 0.05 μ M / CYP2D6 IC₅₀: 1.6 μ M). The dimethyl substitution of compound **12** reduced CYP3A4 and CYP2D6 inhibition 370 and 6-fold while the methoxy substitution of compound **13** reduced CYP3A4 and CYP2D6 inhibition 270 and 8-fold (see Table 1).

Microsomal stability was then re-determined using a 10-fold lower concentration of substrate than initially employed. It is worthy of note that the reduced concentration resulted in a CL_{int} of ~99 μ L/min/mg for compound **11**, 10-fold higher than the CL_{int} estimated in experiments with the 0.5 μ g/mL substrate concentration. Similarly, the reduced concentration of compound **12** resulted in an estimated CL_{int} of ~173 μ L/min/mg, 4-fold faster than in the initial microsome incubations. In order to improve the metabolic stability of the leads while simultaneously reducing the potency of CYP inhibition, it was necessary to first identify the preferred routes of biotransformation for these new derivatives.

A demethylation product metabolite of compound **12** was identified following incubation with mouse liver microsomes. In addition, mono-hydroxylation metabolites were also detected. When compound **12** was incubated in the presence of both Phase I and Phase II cofactors, the phenolic metabolite undergoes subsequent glucuronide conjugation (see Figure 2).

Once it was determined that the methoxy group was a major site of metabolic vulnerability, additional derivatives of compound **12** were synthesized bearing less reactive substituents at that position to diminish the formation of these demethylated metabolites. The crystal structure data suggests that the 2-methoxy-phenyl occupies a tight, predominately hydrophobic pocket consisting of Leu 20, Ser 49, Ile 50 and the cofactor, NADPH. With limited physical space to modify the compound, two strategies were envisioned to reduce or prevent the formation of the demethylation product: 1) modification of the methoxy group through deuteration or fluorination and 2) replacement of the methoxy group altogether.

Compound **14**, a deuterated derivative of **12**, and compound **15**, a fluorinated derivative of **12**, were designed to potentially slow the demethylation route and gave CL_{int} values of ~ 154 and ~ 22 $\mu\text{L}/\text{min}/\text{mg}$, respectively. The pharmacokinetic effects of removing the metabolic liabilities present in compound **11** were investigated through the synthesis of three analogs; hydro-substituted (compound **16**), chlorine-substituted (compound **17**), and fluorine-substituted (compound **18**) phenyl derivatives. Where the CL_{int} for compound **16** was calculated to be ~ 70 $\mu\text{L}/\text{min}/\text{mg}$, a modest 2.5-fold decrease from compound **12**, the chloro- and fluoro-derivatives recorded clearances of ~ 25 and ~ 28 $\mu\text{L}/\text{min}/\text{mg}$, respectively (see Table 1). The 2-chlorophenyl derivative, compound **17**, demonstrated virtually no CYP inhibition, a significantly extended half-life, maintained potent antibacterial activity, and was selected for further testing.

Human hepatocyte stability for compound 17. The metabolic stability of our most promising compound, **17**, was subsequently determined in human hepatocytes to provide context for data collected in *in vitro* mouse models and predicted human clearance. The resulting half-life was 180 minutes and corresponds to an CL_{int} of ~ 8 $\mu\text{L}/\text{min}/10^6$ cells, an $CL_{int,app,scaled}$ of ~ 19 $\text{mL}/\text{min}/\text{kg}$, and subsequent extrapolation to an hepatic clearance of ~ 10 $\text{mL}/\text{min}/\text{kg}$.

Metabolite identification for compound 17 in human and mouse hepatocytes. Prior to *in vivo* evaluation, we identified the major metabolites of compound **17** in mouse and human hepatocytes to confirm that we did not introduce unexpected metabolites. Based on the UV trace of the metabolites generated, the major metabolic pathway for compound **17** in mouse and human hepatocytes was oxidation, either hydroxylation or N-oxidation (see Figure 3). In the high-resolution full scan, the parent $[M+H]^+$ was observed at m/z 406.1746 which is identical to the calculated value for compound **17**. Results from incubation with mouse hepatocytes mirrored those from human hepatocyte incubation. For both experiments, metabolite ions were observed at m/z 438 (bis-hydroxylation), m/z 422 (mono-hydroxylation or N-oxidation), and m/z 436 (methyl conversion to carboxylic acid). The fragmentation patterns of the metabolites were distinct from that of the parent, and either the fragment ion at m/z 189,

corresponding to the diaminopyrimidine ring and propargyl linker, or the fragment ion m/z 244, corresponding to the propargyl methyl and biphenyl system, was used to identify and assign the masses for metabolites and the parent compound. The N-oxide and hydroxylation metabolites were assigned by either the loss of 16 mass units, consistent with N-oxide fragmentation by loss of oxygen, or the loss of 18 mass units indicative of hydroxyl release. We were able to discern that hydroxylation occurs at the propargyl methyl in mouse hepatocytes. Likewise, it was possible to observe conversion of a methyl to a carboxylic acid ortho to the pyridine nitrogen in human hepatocytes. There were no diagnostic fragments that could aid in identifying the location of the other hydroxylation products even though each had distinct retention times. The proposed metabolic pathway is summarized in Figure 4, and the MS² and MS³ spectra are available in Supplemental Figures 1-11.

***In vivo* pharmacokinetics for compound 19.** For comparison to compound **11**, compound **19**, the single S-isomer of racemate **17**, was synthesized for *in vivo* analysis. The plasma profiles of compound **19** were analyzed following IP and oral doses of 5 mg/kg via non-compartmental analysis using a linear trapezoidal method (see Supplemental Figure 15-16). IP administration yielded a C_{max} of 4.1 µg/mL, AUC of 838 min*µg/mL, CL of 6.0 mL/min/kg, and half-life of 69 minutes. When administered orally at 16 mg/kg, the C_{max}, AUC, and half-life were 0.4 µg/mL, 156 min*µg/mL, and 4.5 hours giving a bioavailability of 18.6%.

Time-kill assays with compound 19. Time-kill curve profiles were determined for compound **19** at 1x, 5x, 10x, and 100x MIC and the results are summarized in Figure 5. Overall, all concentrations above the MIC demonstrated similar bactericidal activity at 12 hours, however, there was significantly faster bacterial killing at concentrations >10x MIC. When exposed to 100x the MIC, the bacterial population was reduced ~40% within four hours, whereas it took eight hours to reach the same level at lower concentrations.

DISCUSSION

In this report we describe some of the challenges faced in the development of new antifolate antibiotics. We determined that our *in vitro* pharmacokinetic model was biased to select for strong CYP inhibitors and suggested artificially long half-lives. After successfully adjusting the assay to better represent *in vivo* conditions, we were able to design compounds with minimal CYP inhibition and ideal pharmacokinetic profiles. Use of high-resolution crystal structures allowed us to do this in an extremely efficient manner without compromising antibacterial activity, demonstrating that structure-based design leveraged with metabolism data (sites and rates) can be combined in the design of superior analogues.

Previous work proved compound **11** had exceptional antibacterial activity against multidrug resistant *S. aureus*, and initial *in vitro* pharmacokinetic data indicated potential for successful *in vivo* studies with a clearance of ~10 $\mu\text{L}/\text{min}/\text{mg}$ of mouse microsomal protein (Keshipeddy et al., 2015). However, the resulting *in vivo* clearance was ~54 $\text{mL}/\text{min}/\text{kg}$, higher than expected and not practicable for *in vivo* infection models. To explain the discrepancies between the *in vitro* and *in vivo* datasets, it was hypothesized that the pyridine moiety of compound **11** (or, potentially, the corresponding N-oxide metabolite) could be inhibiting CYP enzymes *in vitro* and producing an artificially long *in vitro* half-life due to saturation of metabolism. Thus, it is possible that the off-target activity of compound **11** was, itself, responsible for the divergence between the *in vitro* and *in vivo* clearance measurements. Crystal structure data of *S. aureus* DHFR with compound **11** guided the synthesis of compounds **12** and **13** to test this hypothesis.

The metabolite profile of compound **10** indicated there are four major metabolites: N-oxidation and hydroxylation of the diaminopyrimidine ring, demethylation of the 2'-methoxy group, and N-oxidation of the pyridine ring (Zhou et al., 2012). Sites of biotransformation on the diaminopyrimidine ring cannot be modified as this functionality is responsible for key hydrogen bonds deep within the active site; however, as the pyridine ring and 2'-methoxy group do not make crucial contacts with the enzyme they are ideal for chemical modification to modulate pharmacokinetic parameters.

Crystal structure analysis of *S. aureus* DHFR complexed with compound **11** indicated that four hydrophobic residues (Leu 20, Leu 28, Ile 50, and Leu 54) could accommodate substitutions adjacent to the nitrogen of the pyridine ring. Two new analogs, **12** and **13**, which contain a 2,6-dimethylpyridyl or 2-methoxypyridyl ring, respectively, were synthesized. Computationally, the dimethyl and methoxy substitutions were predicted to increase ligand-target interactions through enhanced van der Waals contacts. Additionally, these modifications were not expected to disrupt the hydrogen bonding network with Arg 57 through an active site water. As anticipated, these substitutions were well tolerated with regard to antibacterial activity, yielding potent MIC values of 0.156 µg/mL.

Evaluation of structure-activity relationships and metabolite identification data of compound **12** confirmed that adding bulky substituents adjacent to the pyridyl nitrogen not only eliminated CYP inhibition but also completely abrogated the N-oxide metabolite formation. Interestingly, as CYP inhibition was reduced, the *in vitro* clearance of lead compound **12** remained unchanged if not enhanced as compared to compound **11**. Metabolite identification studies indicated that 2-methoxyphenyl demethylation was the primary metabolite. A small but focused series of five compounds were synthesized predicated on the structural analysis of metabolites and the modes of binding to *S. aureus* DHFR to decrease clearance rates.

Deuterated and fluorinated derivatives, **14** and **15**, were designed to slow or prevent formation of the demethylated metabolites. Deuteration was an attractive approach as there are minimal differences between the physiochemical chemical properties of hydrogen and behavior in the DHFR active site is expected to be the same. The effects of substituting hydrogens for deuterium isotopes has gained interest as an approach to reduce the reactivity and slow the biotransformation of drugs (Guengerich, 2017). In the case of deutetrabenazine, approved in 2017 as the first deuterated therapeutic, two deuterated methoxy groups are proposed to slow the generation of the hydroxyl metabolite to a useful degree (Schmidt, 2017). However, the deuteration of compound **12** showed minimal benefit, imparting little to no effect on the *in vitro* clearance (compound **12** CL_{int}: 8 minutes; compound **14**, the deuterated derivative, CL_{int}: 9 minutes).

The trifluoromethyl substitution has become fairly commonplace in therapeutics as it is known to impart metabolic stability when replacing a methyl group, setting precedent for the synthesis of compound **15** (Feng et al., 2016; Wang et al., 2013). The strong electronegativity of the trifluoromethoxy had a profound effect on metabolic stability, increasing half-life nearly 8-fold and eliminating CYP inhibition (CYP3A4 IC_{50} : $>50 \mu M$, CYP2D6 IC_{50} : $>50 \mu M$).

Three compounds were designed to test the effects of replacing the methoxy group of compound **12** on the observed *in vitro* clearance. An unsubstituted phenyl derivative resulted in a modest 2.5-fold decrease in CL_{int} , likely due to the propensity for exposed phenyl rings to be CYP substrates. Chlorinated (compound **17**) and fluorinated (compound **18**) derivatives were synthesized as substituting aromatic rings with electronegative atoms are known to slow oxidative metabolism (Wang et al., 2013). Crystal structure data indicates that Ser 49 participates in a hydrogen bond with the oxygen of compound **11**, and with evidence suggesting that halogens may act as weak hydrogen bond acceptors, it was anticipated that chlorine and fluorine substitutions would have minimal impact on ligand binding (Lin et al., 2017).

This had a marked effect on the *in vitro* clearance, decreasing it ~4 fold for compounds **17** and **18**, respectively. *In vitro* estimations in mouse liver microsomes correspond with intrinsic clearance calculated in human hepatocytes (compound **17** $CL_{int,app,scaled}$: $\sim 19 \mu L/min/kg$). Compound **19**, the corresponding enantiomer of **17**, was synthesized not only for direct *in vivo* comparison to compound **11**, but also because crystal structure data suggests this enantiomer predominately occupies the active site of DHFR. Our conclusions from *in vitro* experiments translated to improvements *in vivo* as half-life, AUC, and CL improved 3-, 3-, and 9-fold when comparing IP data (see Table 2).

While an 8-fold loss in potency, as assessed by MIC, was observed for compound **19** compared to compound **11**, the pharmacodynamic profile of compound **19** provides powerful insight into predicting efficacy. Time-kill curve analysis indicate that compound **19** demonstrates concentration-dependent antibacterial activity at concentrations $>10x$ MIC. In this case, peak/MIC and AUC/MIC are the important pharmacodynamic descriptors. If given by the intraperitoneal route, the peak/MIC is 26 and the

AUC/MIC is over 5,000. For context, aminoglycosides, a staple in several antibiotic regimens, demonstrate concentration-dependent antibacterial activity and a >90% rate is associated with a peak/MIC ratio of ≥ 12 (Moore et al., 1987). Likewise, fluoroquinolones, another class of powerful concentration-dependent antibiotics, are associated with a 100% microbiological response if they achieve an AUC/MIC ratio or >33 (Ambrose et al., 2001). In the case that plasma levels are $\leq 10 \times$ MIC, time-dependent antibacterial activity and $\text{time} > \text{MIC}$ is the pharmacodynamic property that correlates with efficacy. With the significantly improved half-life, plasma levels are maintained for nearly ten hours above the MIC indicating effective concentrations can be maintained.

In this report, we describe the further optimization of propargyl-linked antifolates as potential new antibiotic agents targeting several of the most important pathogenic bacteria. Key to the success of these efforts was the availability of a high-resolution crystal structure of the lead agent in complex with the bacterial target. Analysis of the metabolic profile in the context of this structure allowed us to design and evaluate a small number of new analogs constructed to limit major metabolic liabilities while maintaining strong interactions with the target, this maintaining strong antibacterial activity while extending exposure to the agent.

ACKNOWLEDGMENTS

The authors thank Dr. Nathan Wiederhold's research group at The University of Texas Health Science Center at San Antonio (UTHSCSA) for determining the *in vivo* pharmacokinetic profile of compound **11**. Metabolite identification for compound **12** was conducted at the Yale School of Medicine Proteomics Center, New Haven, CT, with the help of Dr. Tukiet Lam. Additionally, this research used resources at the Stanford Synchrotron Radiation Lightsource, SLAC National Accelerator Laboratory, which supported by the U.S. Department of Energy, Office of Science, Office of Basic Energy Sciences under Contract No. DE-AC02-76SF00515.

AUTHORSHIP CONTRIBUTIONS

Participated in research design: Lombardo, G-Dayanandan, Obach, Priestley, Wright

Conducted experiments: Lombardo, G-Dayanandan, Zhou, Reeve, Alverson, Barney, Walker, Hoody, Priestley

Contributed new reagents or analytic tools: G-Dayanandan, Keshipeddy, Si, Obach

Performed data analysis: Lombardo, G- Dayanandan, Obach, Wright

Wrote or contributed to the writing of the manuscript: Lombardo, G-Dayanandan, Wright

REFERENCES

- Adams PD, Afonine PV, Bunkóczi G, Chen VB, Davis IW, Echols N, Headd JJ, Hung LW, Kapral GJ, Grosse-Kunstleve RW, McCoy AJ, Moriarty NW, Oeffner R, Read RJ, Richardson DC, Richardson JS, Terwilliger TC, Zwart PH (2010) PHENIX: a comprehensive Python-based system for macromolecular structure solution. *Acta Crystallogr D Biol Crystallogr* 66.2: 213-221.
- Ambrose PG, Grasela DM, Grasela TH, Passarell J, Mayer HB, and Pierce PF (2001) Pharmacodynamics of fluoroquinolones against *Streptococcus pneumoniae* in patients with community-acquired respiratory tract infections. *Antimicrob Agents Chemother* 45.10: 2793-2797.
- CLSI (2015) *M07-A10: Methods for Dilution Antimicrobial Susceptibility Tests for Bacteria That Grow Aerobically; Approved Standard*, 10th ed. Clinical and Laboratory Standards Institute, Pennsylvania.
- Craig W (1993) Pharmacodynamics of antimicrobial agents as a basis for determining dosage regimens. *Eur J Clin Microbiol Infect Dis* 12.1: S6-8.
- Emsley P, Lohkamp B, Scott WG, and Cowtan K (2010) Features and development of Coot. *Acta Crystallogr D Biol Crystallogr* 66.4: 486-501.
- Feng P, Lee KN, Lee JW, Zhan C, and Ngai MY (2016) Access to a new class of synthetic building blocks via trifluoromethoxylation of pyridines and pyrimidines. *Chem Sci* 7.1: 424-429.
- Frey KM, Liu J, Lombardo MN, Bolstad DB, Wright DL, and Anderson AC (2009) Crystal structures of wild-type and mutant methicillin-resistant *Staphylococcus aureus* dihydrofolate reductase reveal an alternate conformation of NADPH that may be linked to trimethoprim resistance. *J Mol Biol* 387.5: 1298-1308.
- Guengerich FP (2017) Kinetic Deuterium Isotope Effects in Cytochrome P450 Reactions. *Methods Enzymol* 596: 217-238.

- Jacobs MR (2001) Optimisation of antimicrobial therapy using pharmacokinetic and pharmacodynamic parameters. *Clin Microbiol Infect* 7.11: 589-596.
- Keshipeddy S, Reeve SM, Anderson AC, and Wright DL (2015) Nonracemic Antifolates Stereoselectively Recruit Alternate Cofactors and Overcome Resistance in *S. aureus*. *J Am Chem Soc* 137.28: 8983-90.
- Levison ME and Levison JH (2009) Pharmacokinetics and pharmacodynamics of antibacterial agents. *Infect Dis Clin North Am* 23.4: 791-815, vii.
- Lin FY and MacKerell Jr, AD (2017) Do Halogen–Hydrogen Bond Donor Interactions Dominate the Favorable Contribution of Halogens to Ligand–Protein Binding? *The Journal of Physical Chemistry B* 121.28: 6813-6821.
- Lombardo MN, G-Dayananandan N, Wright DL, and Anderson AC (2016) Crystal Structures of Trimethoprim-Resistant DfrA1 Rationalize Potent Inhibition by Propargyl-Linked Antifolates. *ACS Infect Dis* 2.2: 149-56.
- McCoy AJ, Grosse-Kunstleve RW, Adams PD, Winn MD, Storoni LC, and Read RJ (2007) Phaser crystallographic software. *J Appl Crystallogr* 40.4: 658-674.
- Moore RD, Lietman PS, and Smith CR (1987) Clinical response to aminoglycoside therapy: importance of the ratio of peak concentration to minimal inhibitory concentration. *J Infect Dis* 155.1: 93-9.
- Otwinowski Z and Minor W (1997) Processing of X-ray diffraction data collected in oscillation mode. *Methods Enzymol* 276: 307-26.
- Schmidt C (2016) First deuterated drug approved. *Nat Biotechnol* 35.6: 493-494.
- Scocchera E, Reeve SM, Keshipeddy S, Lombardo MN, Hajian B, Sochia AE, Alverson JB, Priestley ND, Anderson AC, and Wright DL (2016) Charged Nonclassical Antifolates with Activity Against Gram-Positive and Gram-Negative Pathogens. *ACS Med Chem Lett* 7.7: 692-6.

Schüttelkopf AW and van Aalten DM (2004) PRODRG: a tool for high-throughput crystallography of protein-ligand complexes. *Acta Crystallogr D Biol Crystallogr* 60.8: 1355-63.

Sun H, Veith H, Xia M, Austin CP, and Huang R (2011) Predictive models for cytochrome P450 isozymes based on quantitative high throughput screening data. *Journal of chemical information and modeling* 51.10: 2474-2481.

Wang J, Sánchez-Roselló M, Aceña JL, del Pozo C, Sorochinsky AE, Fustero S, Soloshonok VA, and Liu H (2013) Fluorine in pharmaceutical industry: fluorine-containing drugs introduced to the market in the last decade (2001-2011). *Chem Rev* 114.4: 2432-506.

Zhou W, Viswanathan K, Hill D, Anderson A, and Wright D (2012) Acetylenic linkers in lead compounds: a study of the stability of the propargyl-linked antifolates. *Drug Metab Dispos* 40.10: 2002-8.

FOOTNOTES

This work was supported by the National Institutes of Health [Grant AI11957].

*These authors contributed equally to this work.

¹Department of Pharmaceutical Sciences, University of Connecticut, 69 N. Eagleville Rd., Storrs, CT
06269

²Pfizer Worldwide Research & Development, Pharmacokinetics, Dynamics, and Metabolism, Groton, CT
06340

³Department of Chemistry and Biochemistry, The University of Montana, Missoula, MT 59812

FIGURE LEGENDS

Figure 1. Crystal structure of *S. aureus* DHFR (cyan) in complex with compound **11** (green). **11** makes conserved hydrogen bonds with Leu 5 and Asp 27 through the diaminopyrimidine ring and hydrophobic residues as well as significant van der Waals contacts with Leu 20, Ser 49, Ile 50, and Phe 92. PDB ID: 6ND2.

Figure 2. The proposed metabolic scheme for compound **12** following incubation with mouse liver microsomes.

Figure 3. The UV trace at 284 nM for compound **17** metabolite identification in mouse and human hepatocytes. (a) Incubation with human hepatocytes indicates there are ten distinct metabolites: four m/z 438 (double hydroxylation products); three m/z with MS-2 data indicating a hydroxylation product; two m/z 422 with MS-2 data indicating N-oxide products; one m/z 436 with MS-2 data indicative of methyl conversion to a carboxylic acid. MS-2 spectra are provided in the supplemental materials. (b) Similarly, mouse hepatocyte incubation indicates there are nine distinct metabolites: three m/z 438 (double hydroxylation products); two m/z 422 with MS-2 data indicating a hydroxylation product; two m/z 422 with MS-2 data indicating N-oxide products; one m/z 436 with MS-2 data indicative of methyl conversion to a carboxylic acid

Figure 4. The proposed metabolic pathway for compound **17**.

Figure 5. Time-kill curve determination of *S. aureus* ATCC 43300 exposed to compound **19** at 1x, 5x, 10x, and 100x the MIC. Data suggests that compound **19** demonstrates concentration-dependent bactericidal activity at concentrations >10x the MIC.

TABLES

Table 1. Propargyl-linked antifolates synthesized to reduce CYP inhibition imparted through the unsubstituted pyridine of compound **11**. The intrinsic clearance is reported for the two substrate concentrations tested, 5 $\mu\text{g/mL}$ and 0.5 $\mu\text{g/mL}$.

Scaffold	Compound	Stereo-chemistry	B-ring	C-ring	MIC ($\mu\text{g/mL}$)	MLM CL_{int} ($\mu\text{L}/\text{min}/\text{mg}$)		CYP3A4 (μM)	CYP2D6 (μM)
						5 $\mu\text{g/mL}$	0.5 $\mu\text{g/mL}$		
	10	racemic			0.625	21	-	-	-
	11	<i>S</i>			0.078	10	99	0.05	1.6
	12	racemic			0.156	40	173	3.6	9.8
	13	racemic			0.156	69	-	2.6	13.2
	14	racemic			0.312	-	154	11	12.9
	15	racemic			0.625	-	22	>50	>50
	16	racemic			0.156	-	69	0.5	27.4
	17	racemic			0.312	-	25	43	>50

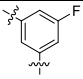
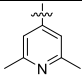
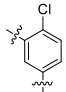
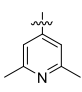
18	racemic			0.625	-	28	5.4	>50
19	S			0.156	-	18	41	>50

Table 2. *In vivo* comparison of compound **11** and compound **19**.

<i>In vivo</i> Data				
Compound	11		19	
	(16 mg/kg)		(5 mg/kg)	
Route	IP	PO	IP	PO
<i>t</i>_{1/2} (min)	19.8	11.4	68.6	272.8
AUC (min* μ g/mL)	294	24.6	838.1	155.8
C_{max} (μ g/mL)	10.16	1.44	4.1	0.4
CL (mL/min/kg)	54.37	–	5.96	–
F (%)	–	8.4	–	18.6

FIGURES

Figure 1.

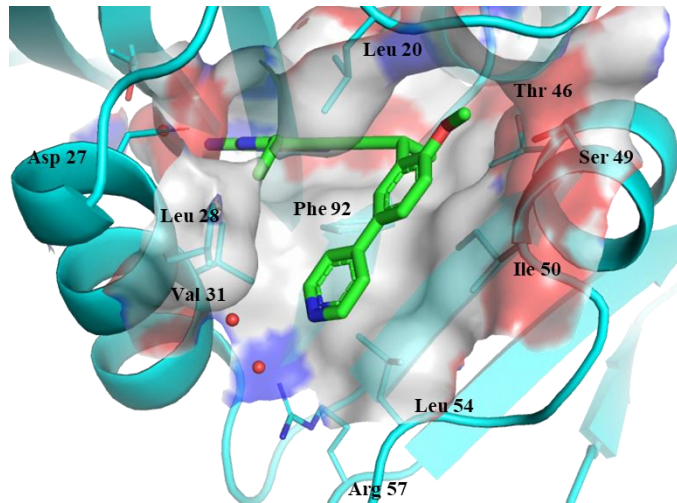


Figure 2

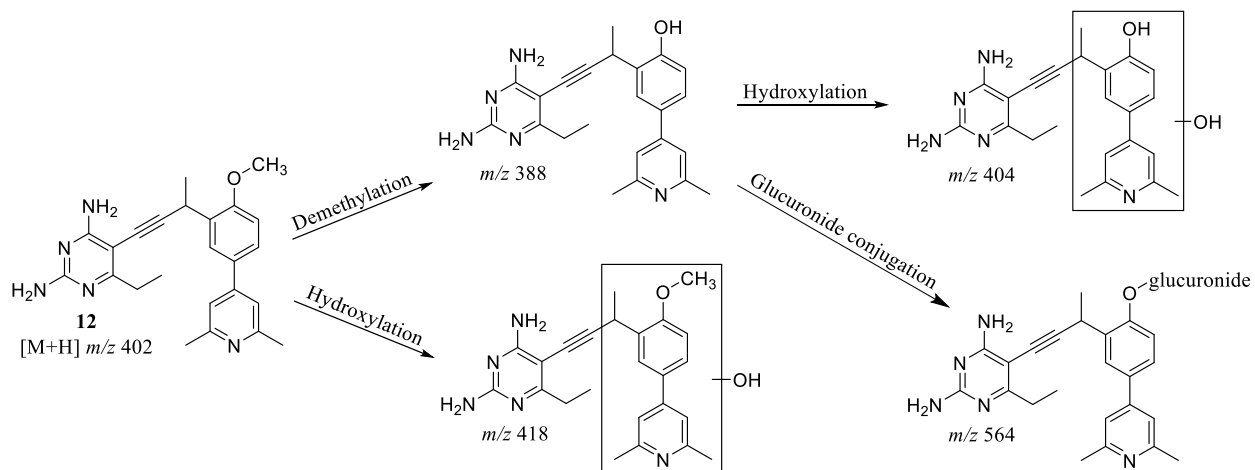


Figure 3.

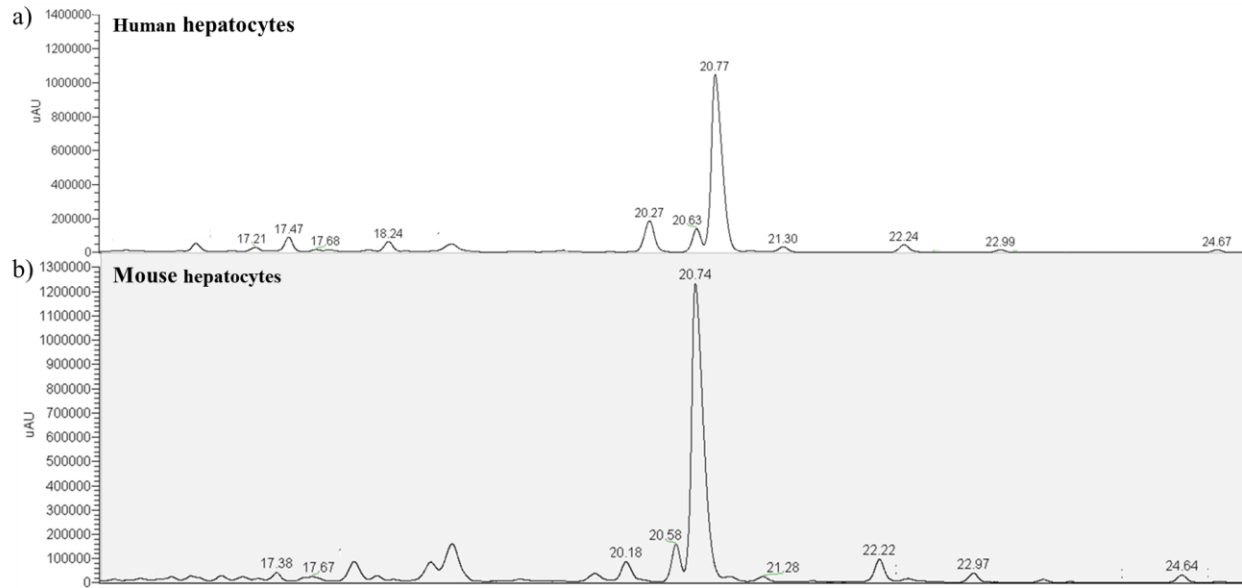


Figure 4.

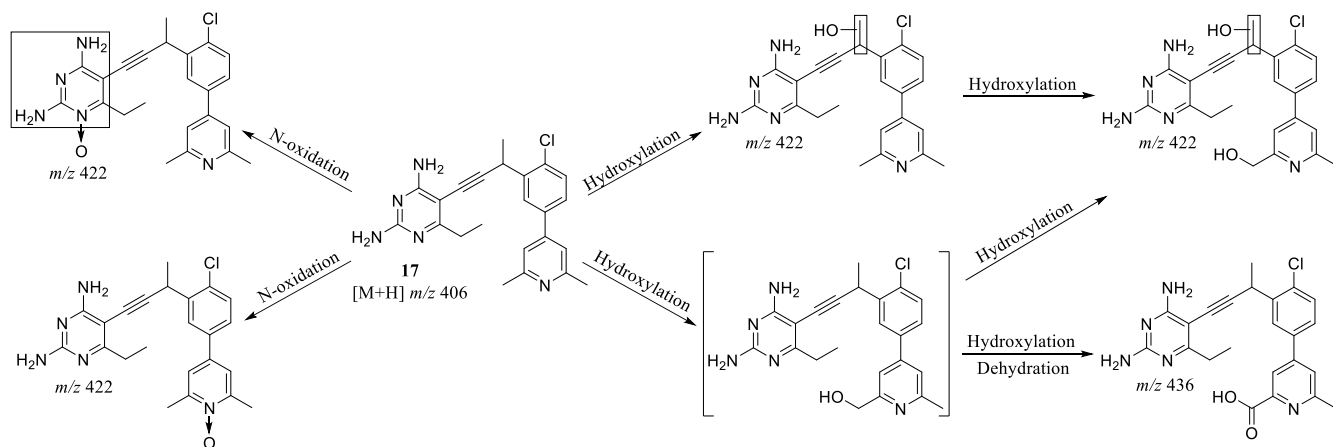


Figure 5.

